Magnetic field effects and excitonic selection rules in monolayer palladium diselenide as a large-gap quantum spin Hall insulator

Ben Li,[*] Juan Zhang,[*] Yujie Xia, Ke Xu, Lei Peng, and Heyuan Zhu
Key Laboratory of Micro- and Nanophotonic Structures (MOE), Department of Optical Science and Engineering, Fudan University, Shanghai 200433, China

Hezhu Shao[†]
College of Electrical and Electronic Engineering, Wenzhou University, Wenzhou 325035, China

Rui Yu[‡]
School of Physics and Technology, Wuhan University, Wuhan 430072, China

Zengxu Wang
College of Science, Nanjing University of Posts and Telecommunications, Nanjing 210003, China

Yuanfeng Xu
School of Science, Shandong Jianzhu University, Jinan 250101, Shandong, China

Hao Zhang[§]
Key Laboratory of Micro- and Nanophotonic Structures (MOE), Department of Optical Science and Engineering, Fudan University, Shanghai 200433, China
and Yiwu Research Institute of Fudan University, Chengbei Road, Yiwu City, Zhejiang 322000, China

(Received 13 November 2022; accepted 10 March 2023; published 5 April 2023)

Quantum spin hall (QSH) effect, a class of quantum state, is promising for dissipationless transport with topologically protected helical edge state. Based on first-principles calculations, we theoretically demonstrate the topological physics of 1H-$PdSe_2$ with a large gap up to 0.24 eV. The band inversion takes place either among the p_z and $p_{x,y}$ orbitals of Se atom or due to spin-orbital coupling under compressive strains. The edge modes exist in the energy gap and can be characterized by an effective edge state Hamiltonian. Based on the derived two-band $\mathbf{k}\cdot\mathbf{p}$ model, we demonstrate the profound phenomena induced by the applied magnetic field effects and optical transitions for chiral fermions, which lead to complicated excitonic selection rules in this topologically nontrivial two-dimensional material. Our results will pave the way for future theoretical and experimental studies on PdX_2 (X = S,Se,Te) monolayers.

DOI: 10.1103/PhysRevB.107.155401

I. INTRODUCTION

Two-dimensional topological insulators (2D TIs), namely quantum spin Hall (QSH) insulators [1,2], have attracted a surge of attention in recent years due to their intriguing physics and promising applications in electronics and spintronics [3,4]. These insulators can support helical edge states inside the bulk band gap, which lead to the dissipationless transport edge channels because of forbidden backscattering under the time-reversal symmetry [5,6]. Such a state was first proposed in graphene [7], but its bulk gap opened by spin-orbit coupling (SOC) is too small [8,9], making its QSH effect unobservable. Same limitation was also presented in HgTe/CdTe [5] and InAs/GaSb [10] quantum-well structures, which requires ultralow operating temperature (below 10 K). Therefore, searching for alternative 2D topological materials with large bulk gaps is important for practical applications.

Recently, many candidates with large band gaps and stable structures have been proposed: chemically modified monolayer honeycomb lattices of Ge [11,12], Sn [13], Bi/Sb [14], bulk square lattice BiF [14], and functionalized MXene [15,16]; new 2D systems, such as Bi_4Br_4 [17], α-Sn (100) film [18], and $ZrTe_5$ ($HfTe_5$) [6], which can be easily exfoliated from layered bulk materials; and transition-metal dichalcogenide in 1T′ structures [19–24]. Since the symmetry-indicator method has been successfully applied in three-dimensional (3D) TIs [25–27], such a method has also been used to build 2D TI databases [28,29], which proposes $PdSe_2$ in the MoS_2 crystal structure (1H phase) may be a promising QSH insulator with large bulk gap. Regarding PdX_2

[*]These authors contributed equally to this work.
[†]hzshao@wzu.edu.cn
[‡]yurui@whu.edu.cn
[§]zhangh@fudan.edu.cn

(X = S, Se, Te), different crystal structures have been reported in several theoretical works: penta-structure with high stability and interesting thermoelectric performance [30,31] and buckled honeycomb lattice with superconductivity and topological states [32]. However, to the best of our knowledge, no efforts have specifically investigated the topological mechanism in 1H-$PdSe_2$.

In this paper, by using first principles calculations, we demonstrate that 1H-$PdSe_2$ is a 2D TI with a large bulk gap. The band gap opened by SOC is 0.24 eV and is enhanced to 0.92 eV within the hybrid Heyd-Scuseria-Ernzerhof (HSE06) functional [33,34]. The phonon calculation indicates that this crystal structure is dynamically stable. The band inversion is found to occur among the p_z and $p_{x,y}$ orbitals of Se atom. Topological phase calculations indicate that its Z_2 invariant is 1 and helical edge states exist in the bulk band gap. Moreover, we construct the $k \cdot p$ Hamiltonian to investigate the edge states and apply the radiation and magnetic field on this Hamiltonian to study the optical properties and the Landau levels.

II. METHODS

First-principle calculations are performed using the Vienna *ab-initio* simulation package (VASP) based on density functional theory (DFT) [35]. The exchange-correlation energy is described by the generalized gradient approximation (GGA) in the Perdew-Burke-Ernzerhof (PBE) parametrization. A plane-wave energy cutoff and energy convergence are set to be 600 eV and 10^{-6} eV with the projector-augmented-wave (PAW) pseudopotential method. We set a $15 \times 15 \times 1$ Γ-centered **k** mesh to carry out the structural relaxation. To avoid artificial interactions between two adjacent atomic layers, the vacuum size is larger than 25 Å. In the following calculations, freestanding $PdSe_2$ monolayer without substrates is under investigation, and thus the effect of substrate is completely neglected. The electronic band structure is further verified by the calculations using the hybrid function (HSE06), with the mixing ratio 25% for the short-range Hartree-Fock exchange and the screening parameter 0.2 $Å^{-1}$. A machine learning algorithm, named Hiphive, with enhanced constraints of acoustic sum rule, rotational symmetry, and Born-Huang condition is used to extract the force constants [36], from which the phonon spectrum can be plotted within the PHONOPY code [37,38]. The maximally localized Wannier functions (MLWFs) using d orbitals of Pd and p orbitals of Se atoms as the initial projections are constructed using the WANNIER90 code [39]. Then the Green's function method [40] is applied on a tight binding model based on MLWFs to calculate the edge state within the WANNIERTOOLS package [41].

III. RESULTS AND DISCUSSION

A. Band inversion and effective k · p Hamiltonian

The optimized crystal structure of monolayer $PdSe_2$ is shown in Fig. 1(a). Monolayer $PdSe_2$ possesses a hexagonal structure, with the Pd atoms and Se atoms located in different layers respectively, similar to the 1H-MoS_2 structure, which can be described by the point group D_{3h}, showing trigonal symmetry and reflection symmetry with respect to the x-y mirror plane. The optimized lattice constant is 4.00 Å. The phonon spectrum possesses no imaginary frequency, as shown in Fig. 1(b), which indicates the thermodynamical stability at low temperatures. Recent work reported the experimental realization of the phase of 2D $PdSe_2$ possessing pentagonal structure layers with orthorhombic lattice and $P2_1/c$ symmetry [42], and the cohesive energies of both orthorhombic and hexagonal phases are −3.58 and −3.32 eV/atom at 0 K, respectively, indicating that these two structural phases are both chemically stable at low temperatures.

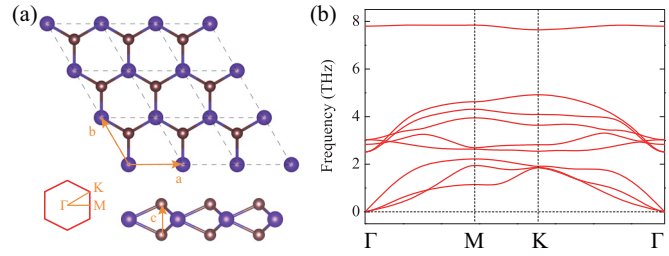

FIG. 1. (a) Atomic structure of $PdSe_2$ in a $3 \times 3 \times 1$ supercell from side view (upper panel) and top view (lower panel), respectively. Large and small spheres represent the Pd and Se atoms, respectively. A color coding is used to distinguish the different atomic species. (b) Phonon spectrum with no imaginary frequency.

The electronic band structures of monolayer $PdSe_2$ is calculated by the PBE method with and without spin-orbit coupling (SOC), as shown in Fig. 2. When SOC is not included, monolayer $PdSe_2$ is gapless with the conduction band (CB) and valence band (VB) touching at the Γ point on the Fermi level. The degenerate states are mainly attributed to $p_x + p_y$ and p_z orbitals of Se atoms. If SOC is taken into consideration, a narrow direct band gap of 0.32 eV is opened up at the Γ point, with a global indirect band gap as large as 0.24 eV.

To obtain a physical understanding of the topological phase, we start from atomic orbitals and consider the effects of crystal field and chemical bonding on the energy levels at the Γ point. Actually, Pd d orbitals also contribute to the bands

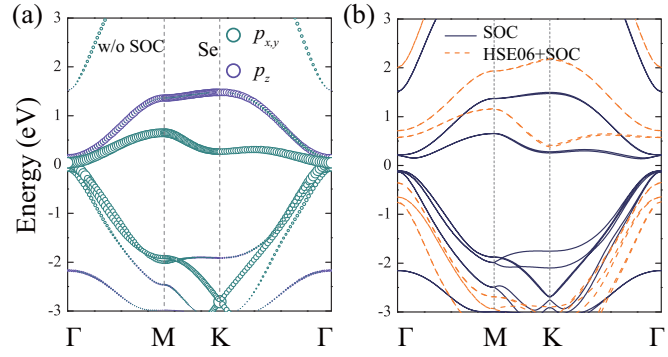

FIG. 2. (a) Band structure of $PdSe_2$ without SOC and atomic orbital weights in the energy bands. The wine and cyan circles represent $p_x + p_y$ and p_z orbitals of Se atoms, respectively. The size of each circle is proportional to the weight of the atomic orbital. (b) Band structure of $PdSe_2$ with SOC (solid) and HSE06+SOC (dashed).

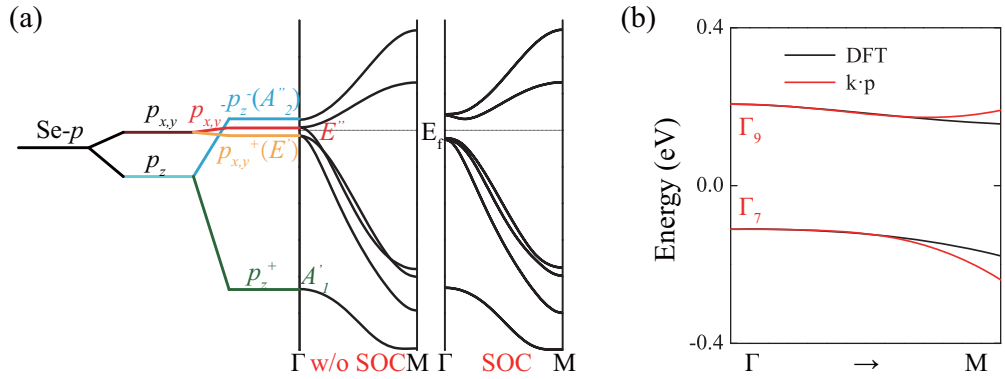

FIG. 3. (a) The schematic illustration of the band inversion mechanism. (b) The energy dispersion obtained from the model Hamiltonian with four bands (red line) is compared with that from the *ab initio* calculation (black line).

around the Fermi level but are mostly occupied. According to the crystal structure, Se atoms align to each other along the c direction. Intuitively, the intralayer coupling between p_z orbitals of Se atoms will play an important role in topological quantum effects. Therefore, we just need to take the Se p orbitals into consideration.

Due to the crystal-field splitting induced by the D_{3h} point-group symmetry, as shown in Fig. 3(a), the triply degenerate p orbitals of Se atoms split into doubly degenerate p_{xy} and singly degenerate p_z orbitals, with the energy of p_z located below that of p_{xy}. Moreover, these orbitals form bonding and antibonding states by the intralayer Se-Se coupling. The bonding and antibonding states of p_z orbitals, denoted by p_z^+ and p_z^- in Fig. 3(a), transform with the A_1' and A_2'' symmetries, respectively, whereas those from p_{xy} [p_{xy}^+ and p_{xy}^- in Fig. 3(a)] transform with E' and E'' symmetries with double degeneracy. The energy splitting caused by chemical bonding states to p_z orbitals of Se atoms lifts $p_z^-(A_2'')$, further crossing the energy of the splitted $p_{xy}^+(E')$, and subsequently, a parity exchange based on the mirror symmetry between occupied and unoccupied bands, forming the so-called band inversion at Γ point. The band inversion between the nondegenerate A_2'' and doubly degenerate E' states not only brings nontrivial band topology to monolayer $PdSe_2$ but also induces a splitting of the doubly degenerate states from Γ to M in the band structure. When the SOC effect is included, $E''(\Gamma_6)$ splits into two new doubly degenerate states, i.e., $\Gamma_6 \bigotimes \Gamma_8 = \Gamma_7 \bigoplus \Gamma_9$, according to the notations of irreducible representations (irreps) of the double point group of D_{3h} [43]. Therefore, a small band gap of 320 meV around Fermi level is opened by introducing the spin degree of freedom, which is also the SOC strength of Se atoms. The hybrid functional (HSE06) calculation is also performed to confirm that, the band inversion around the Γ point is kept and the direct band gap at the Γ point is enlarged to 0.92 eV.

To further investigate the topological physics of monolayer $PdSe_2$, we derive a simple effective Hamiltonian to characterize the low-energy bands around the Γ point of the system. We only focus on the low-lying states of the minimum of CB (CBM) and maximum of VB (VBM) at the Γ point with the spin degree of freedom, which possess the irreps of Γ_7 and Γ_9, respectively. The basis functions of Γ_7 and Γ_9 can be transformed into the $|JM_J\rangle$ basis, i.e., $|\frac{3}{2}, \pm\frac{3}{2}\rangle$ and $|\frac{1}{2}, \pm\frac{1}{2}\rangle$, where $\pm$ represents spin-up and spin-down respectively [43]. Therefore, starting from these four basis, a $\mathbf{k}\cdot\mathbf{p}$ Hamiltonian can be constructed according to the theory of invariants [44,45] for the finite wave vector $\mathbf{k}$. The prime symmetry operations $\hat{R}$ of the system are time-reversal symmetry T, mirror symmetry σ_h, twofold rotation symmetry C_2 along the x axis, and three-fold rotation symmetry C_3 along the z axis, and the representations $D(\hat{R})$ of these operations are given by

$$T = \mathcal{K}\cdot i\sigma_y \otimes \mathrm{I}_{2\times 2}, \tag{1a}$$

$$\sigma_h = i\sigma_z \otimes \mathrm{I}_{2\times 2}, \tag{1b}$$

$$C_{2x} = i\sigma_x \otimes \mathrm{I}_{2\times 2}, \tag{1c}$$

$$C_{3z} = \exp\left(i(\pi/3)\sigma_z \otimes \tau_+\right) + \mathrm{I}_{2\times 2} \otimes \tau_-, \tag{1d}$$

where $\mathcal{K}$ is the complex conjugation operator, $\sigma_{x,y,z}$ denotes the Pauli matrices, and $\tau_\pm = (\sigma_z \pm \mathrm{I}_{2\times 2})/2$. With the constraints of $D(\hat{R})H(\mathbf{k})D(\hat{R})^{-1} = H(\hat{R}\mathbf{k})$ and keeping the $\mathbf{k}$ terms up to the quadratic order, we obtain the $\mathbf{k}\cdot\mathbf{p}$ Hamiltonian for the low-energy bands around Γ point,

$$H(\mathbf{k}) = \begin{pmatrix} A + Mk(+)k(-) & Ck(+)^2 + Dk(-) & 0 & 0 \\ Ck(-)^2 - Dk(+) & B + Nk(+)k(-) & 0 & 0 \\ 0 & 0 & A + Mk(+)k(-) & Ck(-)^2 + Dk(+) \\ 0 & 0 & Ck(+)^2 - Dk(-) & B + Nk(+)k(-) \end{pmatrix}, \tag{2}$$

where $k(\pm) = k_x \pm ik_y$. By fitting this model Hamiltonian with the calculated band structure from the DFT calculation, the parameters can be determined as $A = 0.21$ eV, $B = -0.11$ eV, $C = 38.5$ eVÅ^2, $D = 0$, $M = -26.1$ eVÅ^2, and

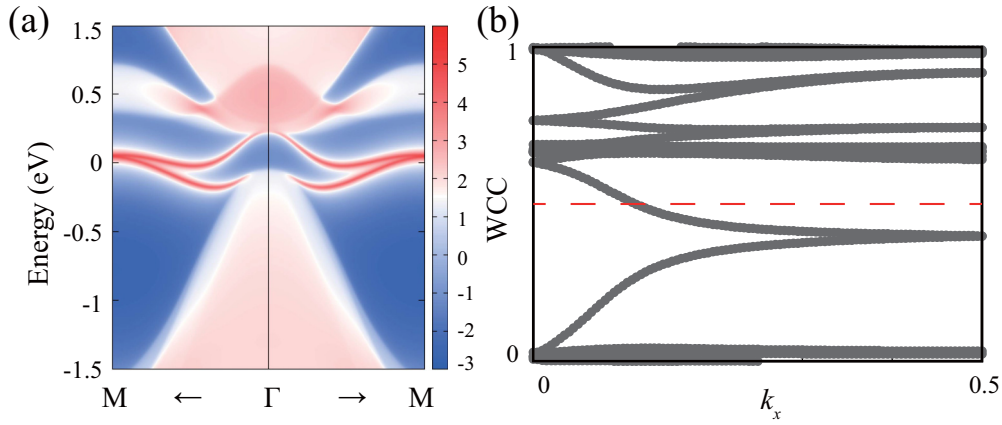

FIG. 4. (a) Topological edge states along the armchair direction. (b) Evolution of Wannier charge centers (WCC) in the Brillouin zone.

$N = -3.2$ eVÅ^2. Since $M < N < 0$, the order of the bands $|\frac{1}{2}, \pm\frac{1}{2}\rangle$ and $|\frac{3}{2}, \pm\frac{3}{2}\rangle$ is inverted around the Γ point ($\mathbf{k} = 0$), which also confirms the topologically nontrivial nature of this Hamiltonian model. The fitted energy band is shown in Fig. 3(b), which is in good agreement with the DFT results around the Γ point in the regime $k_x < 0.05$ Å.

B. Topological edge states

The explicit solution of edge states can be obtained by solving the $\mathbf{k} \cdot \mathbf{p}$ Hamiltonian equation with an open boundary [4]. For simplicity and without loss of generality, we consider a semifinite system ($y > 0$), in which k_x is still a good quantum number, but k_y is not. By replacing k_y with the operator of $-i\partial_y$ and setting $k_x = 0$ in Eq. (2), the 1D Schrödinger equation, i.e., $H(-i\partial_y)\psi = E\psi$, can be solved to obtain two renormalized edge-state wave functions, i.e., $\psi_\uparrow = [{}^{\varphi_0}_{0}]$ and $\psi_\downarrow = [{}^{0}_{\varphi_0}]$. The effective Hamiltonian for edge states can be derived by projecting the bulk Hamiltonian onto these two edge modes. For the leading order k_x term, the 2×2 edge Hamiltonian defined by $H_{\alpha\beta}(k_x) = \langle\psi_\alpha|H(\mathbf{k})|\psi_\beta\rangle$ can be derived as

$$H_{\text{edge}}(k_x) = \begin{pmatrix} A + \frac{M+N}{2}k_x^2 + iDk_x & 0 \\ 0 & B + \frac{M+N}{2}k_x^2 - iDk_x \end{pmatrix}. \tag{3}$$

This analytical result shows that the edge state at the Γ point is not a linear Dirac cone but manifests parabolic shape, which agrees well with the *ab initio* calculations from the WANNIERTOOLS package [41], which is based on the maximally localized Wannier functions (MLWFs) constructed from WANNIER90 code and the use of the surface Green's function method.

As shown in Fig. 4(a), the topologically protected conducting edge states connect the bulk valence and conduction bands, confirming the topologically nontrivial nature of monolayer $PdSe_2$. By tracing the evolution of the Wannier charge centers (WCC) during time-reversal pumping [46], the Z_2 invariant, which is counted by the odd number of the crossings between WCC (gray lines) and the reference line (red line) as shown in Fig. 4(b), is equal to 1, confirming the QSH phase of monolayer $PdSe_2$. We further check the topological invariant by the using the state-of-art SYMTOPO code [47], and the calculated symmetry-based indicator is $Z_3 = 1$, which confirms that monolayer $PdSe_2$ is QSH with the mirror Chern number equal [48] to 1.

C. Strain-engineering topological phase diagrams

It is well known that the physical properties of 2D materials can be effectively tuned by strain. Herein we demonstrate that strain can induce interesting multiple topological phase transitions in the 1H-phase $PdSe_2$ monolayer. We introduce the hydrostatic strains to present the energy levels of p_{xy}^+ and p_z^- orbitals as shown in Fig. 5(a), which can also expound the band inversion process. From compressing to stretching the lattice, as the distance between the Se atoms along the vertical direction increases, the intralayer coupling between p_z orbitals of Se atoms decreases, pushing the p_z^- state upward with respect to p_{xy}^+ state. An energy level crossing point occurs at a critical strain of around -1%, leading to a parity exchange restricted by the mirror symmetry between occupied and unoccupied bands, and a topological phase transition takes place. We further investigate the evolution of electronic structures with SOC against an external strain. As shown in Fig. 5(b), the SOC strength of p_{xy}^- state is insensitive to the strain but decreases slightly with the lattice expanding. While the indirect gap exhibits a sudden change under the compressive strains, since the p_z^- state shifts downward with respect to the Fermi level. Therefore, the system turns to a semimetal with the increase of compressive strains.

As mentioned above, the band inversion in 1H $PdSe_2$ is not due to SOC but caused by the intralayer coupling, so the topological nature should be sensitive to the external strains. However, our topological invariant calculations show that the QSH state always survives in response to the external strains in the range of $\pm 6\%$, not in accordance with the mechanism of band inversion analyzed before. It can be understood that the p_{xy}^- state at the Γ point splits to $P_{\frac{1}{2}}$ (Γ_9) and $P_{\frac{3}{2}}$ (Γ_7) due to SOC, while the $P_{\frac{3}{2}}$ state locates lower than the p_{xy}^+ under the compressive strains larger than 2%, inducing the other band inversion at the Γ point. Therefore, when applying compressive strains larger than 2%, 1H $PdSe_2$ transforms from QSH insulator to QSH semimetal. The topological edge states

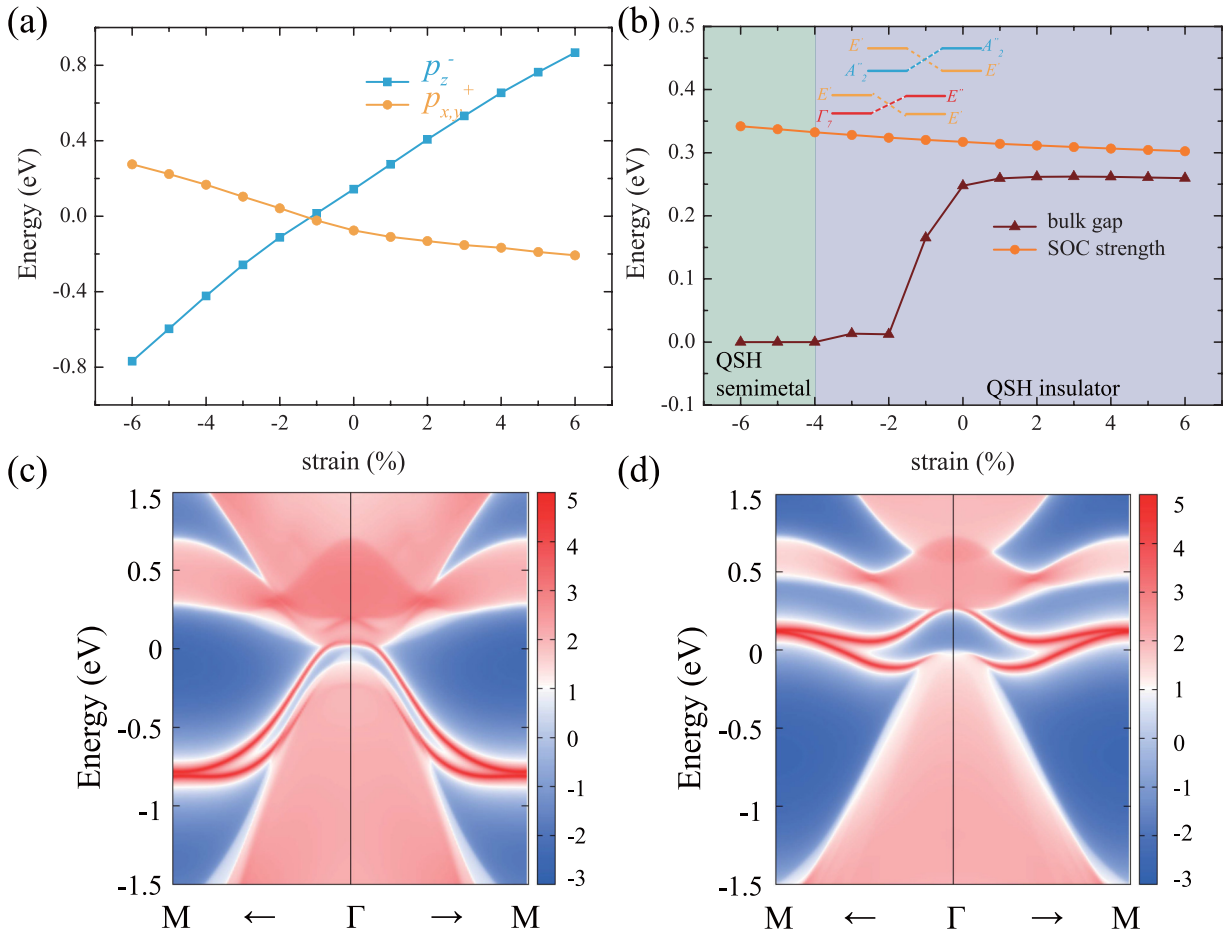

FIG. 5. (a) The energy levels p_{xy}^+ and p_z^- of 1H-$PdSe_2$ at the Γ point under different hydrostatic strains, from compress strains to tensile strains. (b) The calculated bulk gaps of 1H-$PdSe_2$ with SOC under different hydrostatic strains. The gap opened by SOC in the p_{xy}^- state is also demonstrated. The nontrivial QSH states survive under all strain conditions. (c) Topological edge states under compress strain of 2%. (d) Topological edge states under tensile strain of 2%.

under different strains have also been plotted in Figs. 5(c) and 5(d) to prove the QSH phase. The diagram of complete quantum phases versus strains of monolayer $PdSe_2$ has been plotted in Fig. 5(b).

D. Magnetic field effects

Another commonly used experimental manipulation is the application of a magnetic field, so we also investigate the Landau levels (LLs) of this 2D QSH insulator in a uniform magnetic field along the z axis. First, to account for the magnetic effect, the wave vector in the $\mathbf{k}\cdot\mathbf{p}$ Hamiltonian should be modified, i.e., $\mathbf{k} \to -i\nabla + e\mathbf{A}/\hbar$ [49]. In Landau gauge, the vector potential satisfies $\mathbf{A} = (-\mu_0 H y, 0, 0)$. Therefore k_x remains a good quantum number. Then we introduce a pair of ladder operators, i.e., $a = (l_B k_x - y/l_B - \partial_y l_B)/\sqrt{2}$, $a^\dagger = (l_B k_x - y/l_B + \partial_y l_B)/\sqrt{2}$, and $[a, a^\dagger] = 1$. The magnetic length is represented as $l_B = \sqrt{\hbar/e\mu_0 H}$. Finally the low-energy Hamiltonian can be derived as

$$H(\mathbf{k}) = \begin{pmatrix} A + \widetilde{M}(a^\dagger a + 1/2) & \widetilde{C}a^{\dagger 2} + \widetilde{D}a & 0 & 0 \\ \widetilde{C}a^2 - \widetilde{D}a^\dagger & B + \widetilde{N}(a^\dagger a + 1/2) & 0 & 0 \\ 0 & 0 & A + \widetilde{M}(a^\dagger a + 1/2) & \widetilde{C}a^2 + \widetilde{D}a^\dagger \\ 0 & 0 & \widetilde{C}a^{\dagger 2} - \widetilde{D}a & B + \widetilde{N}(a^\dagger a + 1/2) \end{pmatrix}, \tag{4}$$

where $\widetilde{M} = 2M/{l_B}^2$, $\widetilde{C} = 2C/{l_B}^2$, $\widetilde{D} = \sqrt{2}D/l_B$, and $\widetilde{N} = 2N/{l_B}^2$. Based on the following Fermion basis functions,

$$(|+1/2, n+1\rangle, |+3/2, n\rangle, |-1/2, n\rangle, |-3/2, n+1\rangle)^T, \quad n \geqslant 1, \tag{5a}$$

$$(|+1/2, 0\rangle, 0, 0, |-3/2, 0\rangle)^T, \quad n = 0, \tag{5b}$$

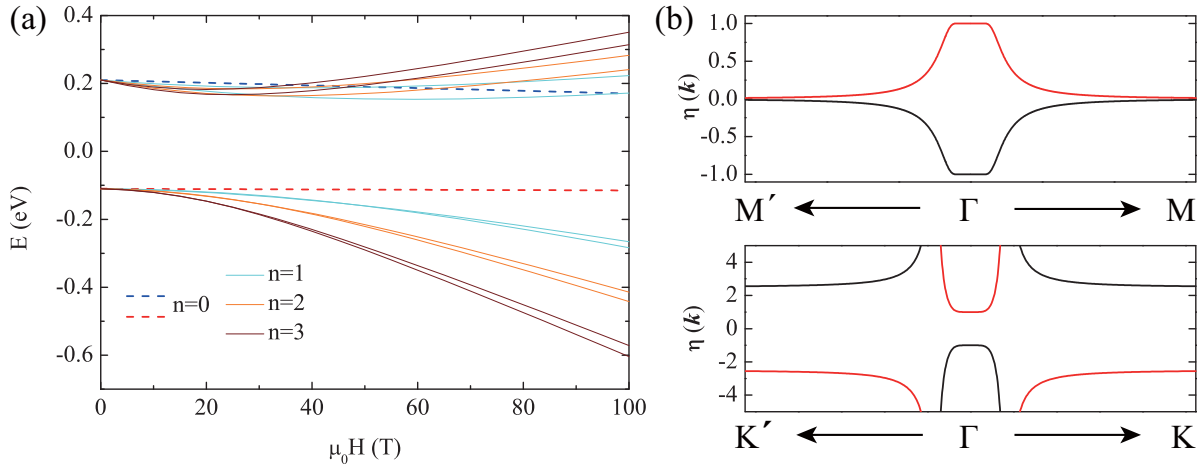

FIG. 6. (a) Landau levels in a magnetic field $\mu_0 H$ along the z axis. The dashed and solid lines represent $n = 0$ and $n \geqslant 1$, respectively. (b) Momentum-resolved circular polarization for spin-up (black) and spin-down (red) electrons.

where $j = \frac{1}{2}/\frac{3}{2}$ denotes the spin quantum number, $\pm$ denotes spin up/down, and n ($n = \langle a^\dagger a \rangle$) is the Landau level quantum number, the energies of LLs can be given by solving the eigen equations

$$E_n, s(n \geqslant 1) = \begin{cases} \frac{1}{2}[u_1 + v_1 + s\sqrt{(u_1 - v_1)^2 + 4\widetilde{C}n\sqrt{n(n+2)}}] \\ \frac{1}{2}[u_2 + v_2 + s\sqrt{(u_2 - v_2)^2 + 4\widetilde{C}n\sqrt{n(n+2)}}] \end{cases}, \tag{6a}$$

$$E_0(n = 0) = \begin{cases} A + \widetilde{M}/2 \\ B + \widetilde{N}/2 \end{cases}, \tag{6b}$$

where $u_1 = A + \widetilde{M}(n + 3/2)$, $v_1 = B + \widetilde{N}(n + 1/2)$, $u_2 = A + \widetilde{M}(n + 1/2)$, $v_2 = B + \widetilde{N}(n + 3/2)$, and $s = \pm 1$ denotes the CB and VB, respectively. The calculated LLs in a magnetic field are shown in Fig. 6(a). The degenerate LLs of $n = 0$ are highlighted. Without considering electron-hole symmetry, the cyclotron frequency for LLs of CB is larger than that of VB, so that the LLs of $n = 0$ will cross at a critical magnetic field, which confirms the QSH state in a weak field [49].

E. Optical properties and excitonic selection rules

The emergence of the nontrivially topological nature of $PdSe_2$ as a QSH with a large band gap also offers a practical platform to explore the optical properties induced by the excitonic behaviors. The eigen energies and wave functions of excitons as the bound electron-hole pairs, which contribute dominantly to the optical properties in two-dimensional materials due to the enhanced reduction of Coulomb screening effects, can be written according to the Bethe-Salpeter equation (BSE) as follows [50–52],

$$A^S_{cv\mathbf{k}}(E_{c\mathbf{k}} - E_{v\mathbf{k}}) + \sum_{\mathbf{k}'} A^S_{cv\mathbf{k}'} \langle cv, \mathbf{k}|K^{eh}|cv, \mathbf{k}'\rangle = \Omega^S A^S_{cv\mathbf{k}}, \tag{7}$$

where $A^S_{cv\mathbf{k}}$ and Ω^S are the envelope function and eigen energy for the Sth exciton, and E_{cv} denotes the eigen energies of $|c\mathbf{k}\rangle$ and $|v\mathbf{k}\rangle$, respectively. K^{eh} is the two-particle electron-hole interaction, including the direct electron-hole attractive screened Coulomb interaction term and the repulsive exchange bare Coulomb term. The excitonic wave function for the Sth exciton can be written as $|S\rangle = \sum_{\mathbf{k}} A^S_{cv\mathbf{k}} |cv, \mathbf{k}\rangle$. The contribution from the Sth exciton to the optical properties can be determined by its oscillator strength O^S, which is written as

$$O^S = \frac{2\left|\sum_{\mathbf{k}} A^S_{cv\mathbf{k}} \mathbf{e} \cdot \langle c\mathbf{k}|\hat{\mathbf{p}}|v\mathbf{k}\rangle\right|^2}{\Omega^S}, \tag{8}$$

where $\mathbf{e}$ and $\hat{\mathbf{p}}$ denote the polarization unit vector of photon and momentum operator, respectively. For photoexcited excitons, the center-of-mass momentum of excitons can be neglected, and the envelope function $A^S_{cv\mathbf{k}}$ can be expanded in the isotropic-model approximation as

$$A^S_{cv\mathbf{k}} = \tilde{A}_m(|\mathbf{k}|)e^{im\phi_k}, \tag{9}$$

where m is the angular momentum and ϕ_k is the angle of $\mathbf{k}$ with respect to k_x axis. The interband optical transition matrix element $\langle c\mathbf{k}|\hat{\mathbf{p}}|v\mathbf{k}\rangle$ can be decomposed into $\mathcal{P}_{k+} = \mathbf{e}_+ \cdot \langle c\mathbf{k}|\hat{\mathbf{p}}|v\mathbf{k}\rangle$ and $\mathcal{P}_{k-} = \mathbf{e}_- \cdot \langle c\mathbf{k}|\hat{\mathbf{p}}|v\mathbf{k}\rangle$, corresponding to the optical coupling to left- and right-circularly polarized photon modes, respectively. Thus, the oscillator strength O^S_m for the Sth exciton with angular quantum number m under circular polarization can be written as

$$O^S_m = \frac{2}{\Omega^S} \sum_{\eta=\pm} \left| \sum_{\mathbf{k}} \tilde{A}_m(|\boldsymbol{k}|)e^{im\phi_k} \mathcal{P}_\eta(\boldsymbol{k}) \right|^2, \tag{10}$$

where the velocity operator $\mathcal{P}_\pm(\mathbf{k}) = \mathcal{P}_x(\mathbf{k}) \pm i\mathcal{P}_y(\mathbf{k})$. For topological nontrivial bands, $\mathcal{P}_x(\mathbf{k})$ and $\mathcal{P}_y(\mathbf{k})$ are generally nonzero and possess different winding numbers.

As mentioned above, the SOC effects in monolayer $PdSe_2$ induce the band gap separating VB and CB, and band

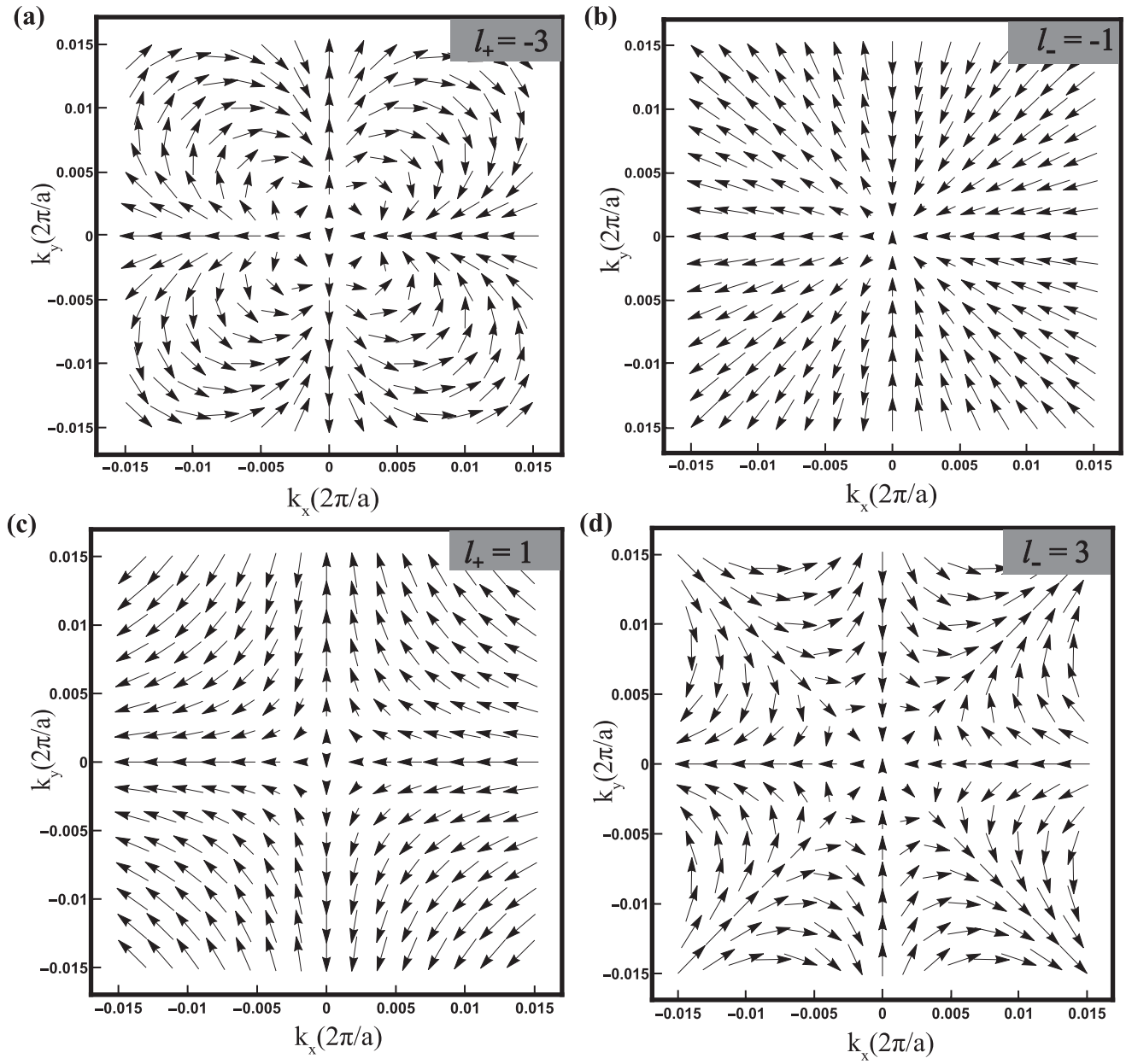

FIG. 7. Angular dependence of Γ-valley interband optical transition matrix elements for spin-up electrons coupled to (a) left- and (b) right-circular polarization, and for spin-down electrons coupled to (c) left- and (b) right-circular polarization.

inversion takes place around the Γ point as well. To describe the excitons formed by the transition of photoexcited electrons around the Γ point, we use a two-band $\mathbf{k}\cdot\mathbf{p}$ model, which is the 2×2 matrix obtained from Eq. (2), as follows,

$$H_s(\boldsymbol{k}) = \begin{pmatrix} A + Mk(+)^2 & Ck(-)^2 + 2isCk_xk_y \\ Ck(-)^2 - 2isCk_xk_y & B + Nk(+)^2 \end{pmatrix}, \tag{11}$$

where $s = \pm 1$ is the spin index indicating spin up and spin down, respectively. Solving the eigensystem of Eq. (11), the eigenstates for conduction band $|c\mathbf{k}\rangle$ and valence band $|v\mathbf{k}\rangle$ can be obtained as follows,

$$\psi_{c,s}(\boldsymbol{k}) = \begin{pmatrix} \Delta + \sqrt{(\Delta)^2 + (2Ck(+)^2)^2} \\ 2C(k(-)^2 - 2isk_xk_y) \end{pmatrix}, \tag{12a}$$

$$\psi_{v,s}(\boldsymbol{k}) = \begin{pmatrix} \Delta - \sqrt{(\Delta)^2 + (2Ck(+)^2)^2} \\ 2C(k(-)^2 - 2isk_xk_y) \end{pmatrix}, \tag{12b}$$

where $\Delta = A - B + (M - N)k(+)^2$ and $\psi_{c/v,s}$ denotes the wave function for CB/VB electrons with the spin index of s, respectively. The optical transition matrix from VB to CB is given by $\mathcal{P}_d(\mathbf{k}) \equiv m_0\langle c\boldsymbol{k}|\frac{1}{\hbar}\frac{\partial H}{\partial k_d}|v\boldsymbol{k}\rangle$ with $d = x/y$ denoting the direction index [53,54]. Thus, for light polarized along the x/y

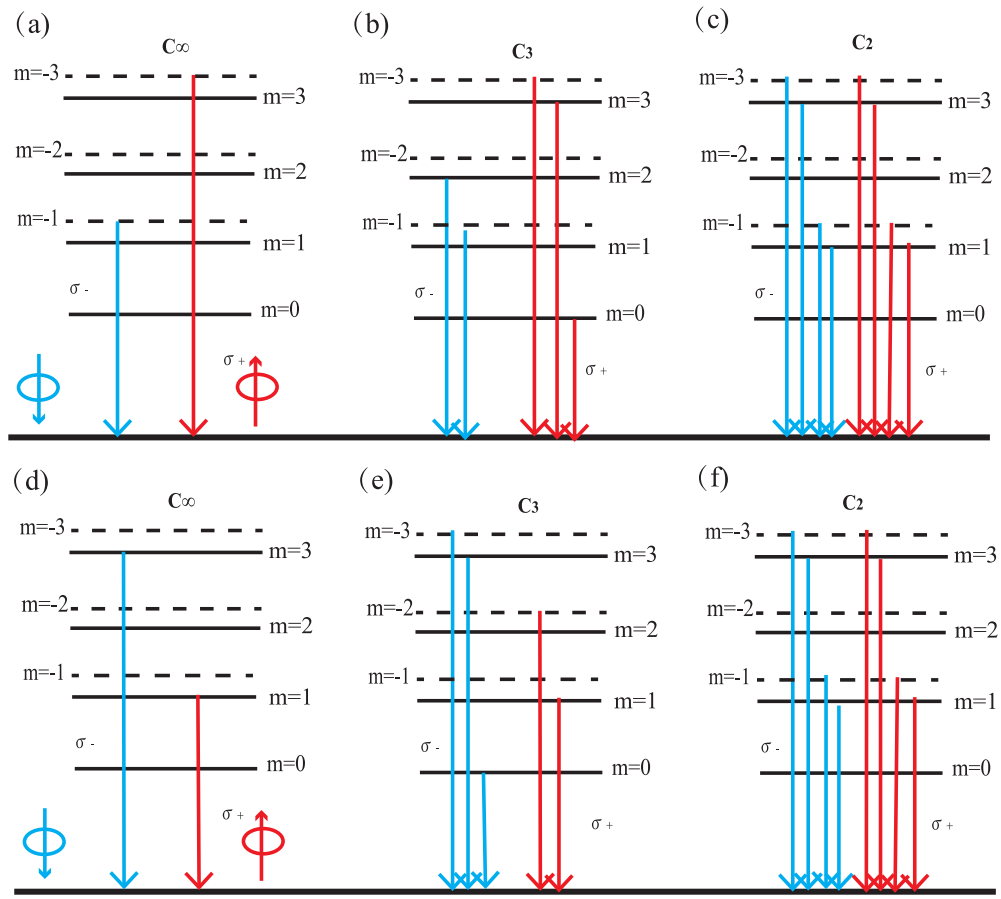

FIG. 8. The excitonic selection rules of the $l_{\pm}$ chiral fermion model with the symmetry is reduced from (a) C_{∞} to (b) C_3 and to (c) C_2 rotational symmetries.

direction, the optical transition matrix element can be derived as

$$\mathcal{P}_x(\boldsymbol{k}) \equiv \frac{m_0}{\hbar}[2Mk_x(\Delta^2-\tau^2)+8C^2\gamma(k_x(N\gamma+\Delta)+isk_y\tau)], \tag{13a}$$

$$\mathcal{P}_y(\boldsymbol{k}) \equiv \frac{m_0}{\hbar}[2Mk_y(\Delta^2-\tau^2)+8C^2\gamma(k_y(N\gamma-\Delta)+isk_x\tau)], \tag{13b}$$

where $\tau = \sqrt{(\Delta)^2+(2Ck(+)^2)^2}$ and $\gamma = k(-)^2 - 2isk_xk_y$. Subsequently, the optical transition matrix element coupled to left- and right-circularly polarized photon modes can be obtained by $\mathcal{P}_{\pm}(\boldsymbol{k}) \equiv \mathcal{P}_x(\boldsymbol{k}) \pm i\mathcal{P}_y(\boldsymbol{k})$ [53]. The degree of circular polarization $\eta(\mathbf{k})$, defined as $\eta(\boldsymbol{k}) \equiv \frac{|\mathcal{P}_+(\boldsymbol{k})|^2-|\mathcal{P}_-(\boldsymbol{k})|^2}{|\mathcal{P}_+(\boldsymbol{k})|^2+|\mathcal{P}_-(\boldsymbol{k})|^2}$, can be calculated and the results are shown in Fig. 6(b), which reveals that the values of circular polarization are opposite for electrons with opposite spin indexes at the Γ point, indicating that the corresponding two Bloch states form a Kramer's pair with opposite orbital magnetic moment. It is worth noting that the degree of circular polarization is equal to unity at the Γ point, but it is close to unity around the Γ point, instead of being quantized near the Γ point. Although the effective Hamiltonian [Eq. (11)] is not valid at M or K points, the curvilinear trend elucidates that the circular dichroisms with opposite crystal momentum are identical because of opposite orbital moment in the presence of time-reversal symmetry [54].

Here the gauge is fixed by demanding that both $|c\mathbf{k}\rangle$ and $|v\mathbf{k}\rangle$ are not singular at the Γ point. According to Eqs. (13), the angular dependence of chiral $\mathcal{P}_+(\mathbf{k})$ and $\mathcal{P}_-(\mathbf{k})$ corresponding to the coupling to left- and right-circularly polarized photon modes can be calculated, and the results are shown in Fig. 7, in which the complex quantities of $\mathcal{P}_+(\mathbf{k})$ and $\mathcal{P}_-(\mathbf{k})$ are represented by the arrows with their lengths proportional to the magnitude and the orientation pointing along the direction with angle of ϕ_k. It should be noted that the off-diagonal terms in the two-band $\mathbf{k}\cdot\mathbf{p}$ Hamiltonian as shown in Eq. (2) are square to the reduced momentum $k_{\pm}$, which means that the velocity matrix element $\mathcal{P}_{\pm}(\mathbf{k})$ satisfies the relation of $\mathcal{P}_{\pm}(\mathbf{k}) \sim e^{-i(w\mp1)\phi_k}$, where the winding number $w = 2$ [55]. As shown in Figs. 7(a) and 7(b), the winding patterns for $\mathcal{P}_{\pm}(\mathbf{k})$ for spin-up electrons indicate that the winding number w for spin-up $\mathcal{P}_{\pm}(\mathbf{k})$ is -2, while the winding patterns for spin-down $\mathcal{P}_{\pm}(\mathbf{k})$ as shown in Figs. 7(c) and 7(d) indicate the spin-down w is 2. Therefore, the angular dependence of $\mathcal{P}_{\pm}(\mathbf{k})$ indicates their angular momentum of $l_{\pm} = w \mp 1$, $l_{\pm}$ for spin-up and spin-down cases are -3, -1, and 1, 3, respectively, which is consistent with the analytical results.

By considering the angular dependence of the velocity matrix elements, the oscillator strength O_m^S for the Sth exciton

can be further written as

$$O_m^S \to \frac{2}{\Omega^S} \sum_{\eta=\pm} \left| \sum_{\mathbf{k}} \tilde{A}_m(|\boldsymbol{k}|) e^{i(m-l_\pm)\phi_k} \right|^2. \tag{14}$$

The oscillator strength O_m^S is nonzero only if $m = l_\pm$. For a symmetry possessing N-fold rotational symmetry, the general excitonic selection rule is

$$m = l_\pm + nN, \tag{15}$$

where n is an integer. As mentioned above, the point group for Γ-point momentum in monolayer $PdSe_2$ is D_{3h}, which includes C_{2x} and C_{3z} rotational symmetry operations.

For isotropic-model approximation with C_∞ symmetry, the excitonic selection rule is $m = l_\pm$, and therefore only the $m = -1$ (σ_-) and $m = -3$ (σ_+) states for spin-up electrons and $m = 3$ (σ_-) and $m = 1$ (σ_+) states for spin-down electrons are bright with the winding number $w = -2$, as shown in Figs. 8(a) and 8(d). $\sigma_\pm$ denotes electrons coupled to left- and right-circularly polarized photon modes, respectively. When considering crystal field, the symmetry reduces to C_3 and C_2. For C_3 symmetry, the excitonic selection rule of Eq. (15) is changed to be $m = l_\pm + 3n$. For spin-up electrons as shown in Fig. 8(b), the $m = 2, -1$ (σ_-) and $m = \pm 3, 0$ (σ_+) are bright, and for spin-down electrons as shown in Fig. 8(e), the $m = \pm 3, 0$ (σ_-) and $m = -2, 1$ (σ_+) are bright. In this case, the optical transitions to s-like states are turned on and have opposite circular polarization compared to the p-like states. Similarly, when the symmetry is reduced to C_2, the excitonic selection rule of Eq. (15) gives more complex results as shown in Figs. 8(c) and 8(f) for spin-up and spin-down electrons, respectively.

IV. CONCLUSION

We have investigated the topological properties of 1H-$PdSe_2$, and find that 1H-$PdSe_2$ monolayer is a QSH insulator with a large gap of 0.24 eV, and the QSH phase is stable against the tensile strains. In this 2D material, the band inversion around the Γ point is induced by the energy shift of p_z^- orbitals due to the intralayer coupling. Under compressive strains larger than 2%, 1H-$PdSe_2$ becomes a QSH semimetal and the band inversion is due to SOC. Topological edge modes also exist, which connect the valence and conduction bands and can be characterized by an effective edge-state Hamiltonian derived from $\mathbf{k} \cdot \mathbf{p}$ Hamiltonian. By applying the magnetic field, the Landau levels are obtained. We also investigate the optical properties of monolayer $PdSe_2$ as a QSH insulator, and finally build the excitonic selection rules for the optical transition of chiral fermions.

ACKNOWLEDGMENTS

H.Z. acknowledges fruitful discussions about the topology physics in condensed matter physics with Hongming Weng and Yi Jiang at Institute of Physics, Chinese Academy of Sciences. This work is supported by the Shanghai Municipal Natural Science Foundation (Grant No. 19ZR1402900), National Natural Science Foundation of China (Grant No. 52272006), Zhejiang Provincial Natural Science Foundation of China (Grant No. LY22A040001), S&T Innovation 2025 Major Special Program of Ningbo (Grant No. 2020Z054), and Wenzhou Municipal Natural Science Foundation (Grant No. G20210016). This work was implemented and deployed on the high-performance computing platform of Nanjing Center of HPC China and Jiangsu HPC and Intelligent Processing Engineer Research Center.

[1] C. L. Kane and E. J. Mele, Phys. Rev. Lett. **95**, 146802 (2005).
[2] B. A. Bernevig and S.-C. Zhang, Phys. Rev. Lett. **96**, 106802 (2006).
[3] M. Z. Hasan and C. L. Kane, Rev. Mod. Phys. **82**, 3045 (2010).
[4] X.-L. Qi and S.-C. Zhang, Rev. Mod. Phys. **83**, 1057 (2011).
[5] B. A. Bernevig, T. L. Hughes, and S.-C. Zhang, Science **314**, 1757 (2006).
[6] H. Weng, X. Dai, and Z. Fang, Phys. Rev. X **4**, 011002 (2014).
[7] C. L. Kane and E. J. Mele, Phys. Rev. Lett. **95**, 226801 (2005).
[8] H. Min, J. E. Hill, N. A. Sinitsyn, B. R. Sahu, L. Kleinman, and A. H. MacDonald, Phys. Rev. B **74**, 165310 (2006).
[9] Y. Yao, F. Ye, X.-L. Qi, S.-C. Zhang, and Z. Fang, Phys. Rev. B **75**, 041401(R) (2007).
[10] I. Knez, R.-R. Du, and G. Sullivan, Phys. Rev. Lett. **107**, 136603 (2011).
[11] C. Si, J. Liu, Y. Xu, J. Wu, B.-L. Gu, and W. Duan, Phys. Rev. B **89**, 115429 (2014).
[12] C.-C. Liu, W. Feng, and Y. Yao, Phys. Rev. Lett. **107**, 076802 (2011).
[13] Y. Xu, B. Yan, H.-J. Zhang, J. Wang, G. Xu, P. Tang, W. Duan, and S.-C. Zhang, Phys. Rev. Lett. **111**, 136804 (2013).
[14] Z. Song, C.-C. Liu, J. Yang, J. Han, M. Ye, B. Fu, Y. Yang, Q. Niu, J. Lu, and Y. Yao, NPG Asia Mater. **6**, e147 (2014).
[15] H. Weng, A. Ranjbar, Y. Liang, Z. Song, M. Khazaei, S. Yunoki, M. Arai, Y. Kawazoe, Z. Fang, and X. Dai, Phys. Rev. B **92**, 075436 (2015).
[16] C. Si, K.-H. Jin, J. Zhou, Z. Sun, and F. Liu, Nano Lett. **16**, 6584 (2016).
[17] J.-J. Zhou, W. Feng, C.-C. Liu, S. Guan, and Y. Yao, Nano Lett. **14**, 4767 (2014).
[18] J. Li and Y. Xu, arXiv:1909.09326v1.
[19] X. Qian, J. Liu, L. Fu, and J. Li, Science **346**, 1344 (2014).
[20] M. A. Cazalilla, H. Ochoa, and F. Guinea, Phys. Rev. Lett. **113**, 077201 (2014).
[21] X.-B. Li, W.-K. Huang, Y.-Y. Lv, K.-W. Zhang, C.-L. Yang, B.-B. Zhang, Y. B. Chen, S.-H. Yao, J. Zhou, M.-H. Lu, L. Sheng, S.-C. Li, J.-F. Jia, Q.-K. Xue, Y.-F. Chen, and D.-Y. Xing, Phys. Rev. Lett. **116**, 176803 (2016).
[22] F. Zheng, C. Cai, S. Ge, X. Zhang, X. Liu, H. Lu, Y. Zhang, J. Qiu, T. Taniguchi, K. Watanabe, S. Jia, J. Qi, J.-H. Chen, D. Sun, and J. Feng, Adv. Mater. **28**, 4845 (2016).
[23] S. Tang, C. Zhang, D. Wong, Z. Pedramrazi, H.-Z. Tsai, C. Jia, B. Moritz, M. Claassen, H. Ryu, S. Kahn, J. Jiang, H. Yan, M. Hashimoto, D. Lu, R. G. Moore, C.-C. Hwang, C. Hwang, Z. Hussain, Y. Chen, M. M. Ugeda *et al.*, Nat. Phys. **13**, 683 (2017).

[24] S. Wu, V. Fatemi, Q. D. Gibson, K. Watanabe, T. Taniguchi, R. J. Cava, and P. Jarillo-Herrero, Science **359**, 76 (2018).
[25] T. Zhang, Y. Jiang, Z. Song, H. Huang, Y. He, Z. Fang, H. Weng, and C. Fang, Nature (London) **566**, 475 (2019).
[26] F. Tang, H. C. Po, A. Vishwanath, and X. Wan, Nature (London) **566**, 486 (2019).
[27] M. G. Vergniory, L. Elcoro, C. Felser, N. Regnault, B. A. Bernevig, and Z. Wang, Nature (London) **566**, 480 (2019).
[28] T. Olsen, E. Andersen, T. Okugawa, D. Torelli, T. Deilmann, and K. S. Thygesen, Phys. Rev. Mater. **3**, 024005 (2019).
[29] D. Wang, F. Tang, J. Ji, W. Zhang, A. Vishwanath, H. C. Po, and X. Wan, Phys. Rev. B **100**, 195108 (2019).
[30] A. D. Oyedele, S. Yang, L. Liang, A. A. Puretzky, K. Wang, J. Zhang, P. Yu, P. R. Pudasaini, A. W. Ghosh, Z. Liu, C. M. Rouleau, B. G. Sumpter, M. F. Chisholm, W. Zhou, P. D. Rack, D. B. Geohegan, and K. Xiao, J. Am. Chem. Soc. **139**, 14090 (2017).
[31] Y.-S. Lan, X.-R. Chen, C.-E. Hu, Y. Cheng, and Q.-F. Chen, J. Mater. Chem. A **7**, 11134 (2019).
[32] C. Liu, C.-S. Lian, M.-H. Liao, Y. Wang, Y. Zhong, C. Ding, W. Li, C.-L. Song, K. He, X.-C. Ma, W. Duan, D. Zhang, Y. Xu, L. Wang, and Q.-K. Xue, Phys. Rev. Mater. **2**, 094001 (2018).
[33] J. Heyd, G. E. Scuseria, and M. Ernzerhof, J. Chem. Phys. **118**, 8207 (2003).
[34] H. J. S. Ge and M. Ernzerhof, J. Chem. Phys. **124**, 219906 (2006).
[35] G. Kresse and J. Furthmüller, Phys. Rev. B **54**, 11169 (1996).
[36] F. Eriksson, E. Fransson, and P. Erhart, Adv. Theory Simul. **2**, 1800184 (2019).
[37] X. Gonze and C. Lee, Phys. Rev. B **55**, 10355 (1997).
[38] A. Togo, F. Oba, and I. Tanaka, Phys. Rev. B **78**, 134106 (2008).
[39] A. A. Mostofi, J. R. Yates, Y.-S. Lee, I. Souza, D. Vanderbilt, and N. Marzari, Comput. Phys. Commun. **178**, 685 (2008).
[40] H. Weng, X. Dai, and Z. Fang, MRS Bull. **39**, 849 (2014).
[41] Q. Wu, S. Zhang, H.-F. Song, M. Troyer, and A. A. Soluyanov, Comput. Phys. Commun. **224**, 405 (2018).
[42] G. Zhang, M. Amani, A. Chaturvedi, C. Tan, J. Bullock, X. Song, H. Kim, D.-H. Lien, M. C. Scott, H. Zhang, and A. Javey, Appl. Phys. Lett. **114**, 253102 (2019).
[43] G. F. Koster, *Properties of the Thirty-two Point Groups* (M.I.T. Press, Cambridge, MA, 1963).
[44] H. Zhang, C.-X. Liu, X.-L. Qi, X. Dai, Z. Fang, and S.-C. Zhang, Nat. Phys. **5**, 438 (2009).
[45] C.-X. Liu, X.-L. Qi, H. Zhang, X. Dai, Z. Fang, and S.-C. Zhang, Phys. Rev. B **82**, 045122 (2010).
[46] R. Yu, X. L. Qi, A. Bernevig, Z. Fang, and X. Dai, Phys. Rev. B **84**, 075119 (2011).
[47] Y. He, Y. Jiang, T. Zhang, H. Huang, C. Fang, and Z. Jin, Chin. Phys. B **28**, 087102 (2019).
[48] J. C. Teo, L. Fu, and C. Kane, Phys. Rev. B **78**, 045426 (2008).
[49] S.-B. Zhang, H.-Z. Lu, and S.-Q. Shen, Sci. Rep. **5**, 13277 (2015).
[50] X. Blase, I. Duchemin, and D. Jacquemin, Chem. Soc. Rev. **47**, 1022 (2018).
[51] B. Peng, H. Zhang, H. Shao, K. Xu, G. Ni, L. Wu, J. Li, H. Lu, Q. Jin, and H. Zhu, ACS Photon. **5**, 4081 (2018).
[52] B. Hou, Y. Zhang, H. Zhang, H. Shao, C. Ma, X. Zhang, Y. Chen, K. Xu, G. Ni, and H. Zhu, J. Phys. Chem. Lett. **11**, 3116 (2020).
[53] D. Xiao, G.-B. Liu, W. Feng, X. Xu, and W. Yao, Phys. Rev. Lett. **108**, 196802 (2012).
[54] W. Yao, D. Xiao, and Q. Niu, Phys. Rev. B **77**, 235406 (2008).
[55] X. Zhang, W.-Y. Shan, and D. Xiao, Phys. Rev. Lett. **120**, 077401 (2018).